



Interfaces coupling of $\text{Co}_8\text{FeS}_8\text{-Fe}_5\text{C}_2$ with elevated d-band center for efficient water oxidation catalysis

Bin Wang ^a, Yuanfu Chen ^{b,*}, Gu Liu ^a, Dawei Liu ^b, Yanfang Liu ^b, Chaoqun Ge ^a, Long Wang ^a, Zegao Wang ^{c,*}, Renbing Wu ^{d,*}, Liuying Wang ^{a,*}

^a *Zhijian Laboratory (Rocket Force University of Engineering), Xi'an 710025, PR China*

^b *State Key Laboratory of Electronic Thin Films and Integrated Devices, University of Electronic Science and Technology of China, Chengdu 610054, PR China*

^c *College of Materials Science and Engineering, Sichuan University, Chengdu 610065, PR China*

^d *Department of Materials Science, Fudan University, Shanghai 200433, PR China*



ARTICLE INFO

Keywords:

Electronic modulation
OER
D-band center
Heterointerface

ABSTRACT

Maximizing the oxygen evolution reaction (OER) catalytic activity of carbon coated core-shell electrocatalysts is significant for the application of water electrolyzers and rechargeable metal-air batteries, yet the modulation of the catalytic properties through interfaces coupling remains challenging. Here, we construct Fe_5C_2 phase interlayered between carbon shell and Co_8FeS_8 core ($\text{Co}_8\text{FeS}_8\text{-Fe}_5\text{C}_2@\text{C}$) for enhancing the alkaline OER catalytic performance. By altering the interlayer phase with Co_{1-x}S as the control sample ($\text{Co}_8\text{FeS}_8\text{-Co}_{1-x}\text{S}@C$), synchrotron X-ray absorption spectroscopy analysis integrated with density functional theory calculations indicate that the induced interfacial electron coupling of $\text{Co}_8\text{FeS}_8\text{-Co}_{1-x}\text{S}$ and $\text{Co}_8\text{FeS}_8\text{-Fe}_5\text{C}_2$ can upshift the d-band center toward Fermi level, optimalize Gibbs free energy for oxygen-containing intermediates, facilitate electron transfer between Co_8FeS_8 and carbon shell. Consequently, the target $\text{Co}_8\text{FeS}_8\text{-Fe}_5\text{C}_2@\text{C}$ catalyst with stronger interface coupling and optimal electron modulation shows an significant overpotential (η_{10}) decrease by 93 mV compared with $\text{Co}_8\text{FeS}_8@\text{C}$, along with a Tafel slop of 48.9 mV dec^{-1} and a long catalytic lifetime, outperforming commercial RuO_2 and other reported analogous catalysts. This work opens up further opportunities of interlayer modification in carbon coated core-shell catalyst to effictivly tailor the d-Band centers for effectively strengthen its catalytic performance.

1. Introduction

Electrocatalytic oxygen evolution reaction (OER) is the important half-cell reaction of charging process in metal-air batteries and oxidation process in water electrolysis [1]. However, the four-proton-coupled electron transfer involving the rigid O-H breaking and O-O forming impose sluggish kinetics on electrocatalytic OER and consequently greatly hamper the overall efficiency [2]. Thus, kinetic enhancement of electrocatalytic OER is an uphill and pressing technical issue in exploring multifunctional electrocatalysts along the path to the large-scale commercialization of the overall water splitting and rechargeable metal-air batteries.

To date, the scarcity and high cost of the precious metal-based materials greatly impede the large-scale practical application despite their high catalytic activity. Hence, substantial effort has been invested in exploring cost-efficiency non-precious metal compounds aimed at

expediting the uphill catalytic process. Among various catalysts, Co_9S_8 has gained widespread attention as a kind of promising OER electrocatalysts due to its optimally filled degenerate orbitals (t_{2g}^6, e_g^1) of Co and low dissociation energy for facile adsorption of oxygen-involving intermediates [3–8]. Nevertheless, the catalytic performance of pristine Co_9S_8 is inferior to that of state-of-the-art OER electrocatalysts due to its drawbacks of mediocre electrical conductivity, limited catalytic active sites, and low intrinsic activity. To optimize the performance of Co_9S_8 , several strategies such as surface modification, morphology manipulation, defect engineering, and embedding with carbon matrix have been applied [9–14]. Based on the fact that Fe ($3d^64s^2$) possesses smaller electronegativity and greater propensity to lose electrons than that of Co ($3d^74s^2$) when forming octahedrons with S anions [15], we had succeeded to synthesize single-phase bimetallic sulfide (Co_8FeS_8) assisted by a novel microwave heating sulfur adsorption strategy in 2019 [16]. Expectedly, the easier electron transfer from Fe species to Co facilitates

* Corresponding authors.

E-mail addresses: yfchen@uestc.edu.cn (Y. Chen), zegao@scu.edu.cn (Z. Wang), rbwu@fudan.edu.cn (R. Wu), lywangxa@163.com (L. Wang).

the Co-O bond cleavage in the Co-O-O configuration, consequently endow Co_8FeS_8 with superior OER catalytic activity than pristine Co_9S_8 and Fe-doped Co_9S_8 , but there is still a certain performance gap compared with the benchmark RuO_2 catalyst.

In light of the interface electron transmission behavior could theoretically modulate the band structure and subsequently achieve a leap in electrocatalytic performance, Co_8FeS_8 -based heterostructure catalyst have been constructed in our follow-up work, and their electrocatalytic OER dynamics are significantly enhanced relative to that of Co_8FeS_8 [17]. Nevertheless, we were usually uncertain about the exact active species of the target catalysts, and the essential reasons for catalytic performance boosting were ambiguously ascribed to the optimal architectural morphology or the synergistic effect between the Co_8FeS_8 -based heterostructure and conductive carbon matrix. While, the precise investigation of catalytic sites at the heterostructure interface was of significant importance for further improving the underlying mechanism of catalytic activity enhancement.

The above-mentioned research status have sparked our motivation to uncover the underlying atomic-level mechanism of catalytic activity enhancement for Co_8FeS_8 from the perspective of d-band center modulation by interfacial engineering. Herein, the target catalysts $\text{Co}_8\text{FeS}_8\text{-Fe}_5\text{C}_2$, bimetal sulfide counterpart ($\text{Co}_8\text{FeS}_8\text{-Co}_{1-x}\text{S}$), and single-metal sulfide analogs (Co_8FeS_8 and Co_{1-x}S) was synthesized based on our previous synthetic protocol. The well-dispersed heterointerfaces and in-depth local atomic structures of Co and Fe sites were revealed. DFT calculations indicate that the interface coupling between Co_8FeS_8 and Fe_5C_2 effectively elevates the d-band center upward to the Fermi level, regulates the adsorption energy with intermediates, and thus enhances OER catalytic kinetics performance. Furthermore, the attached catalytic properties of HER and ORR enable $\text{Co}_8\text{FeS}_8\text{-Fe}_5\text{C}_2@C$ to be functional in overall water splitting and Zn-Air batteries. As expected, the coupled electrolyzer and assembled Zn-Air battery device by use of $\text{Co}_8\text{FeS}_8\text{-Fe}_5\text{C}_2@C$ deliver better performance than commercial noble metal mixed catalysts ($\text{RuO}_2 + \text{Pt/C}$). This work opens up further opportunities of interlayer modification in carbon coated core-shell catalyst to effectively tailor the d-Band centers for promoting electrocatalytic activity and expanding the versatility in multifunctional catalysis.

2. Experimental

2.1. Material synthesis

Preparation of PBAs: 13.5 mmol trisodium citrate dihydrate and 9 mmol cobalt (II) nitrate hexahydrate were mixed into 300 mL of deionized water (DI water) and subsequently ultrasonicated for 5 min to yield a homogeneous solution (labeled No. 1 solution). 6 mmol of potassium ferricyanide (PF) and 9 mmol of dimethylimidazole (MIM) were dissolved in another 300 mL DI water and subsequently ultrasonicated for 5 min to obtain No. 2 solution. The two solutions were then vigorously mixed and stand for 20 h. The indigo precipitate was collected by centrifugation with a mixture of ethanol and DI water to remove the excess sodium citrate and uncoordinated ligands. The prussian blue analogue precursor PBA-2-3 (2-3 denoted the mole ratio of potassium ferricyanide and dimethylimidazole) was then freeze-dried overnight for further use. Additionally, the synthesis process for PBA, PBA-1-3, ZIF were same as that of PBA-2-3 but only with 6 mmol PF, 6 mmol PF and 18 mmol MIM, 18 mmol MIM as ligands, respectively.

Preparation of $\text{Co}_8\text{FeS}_8\text{-Fe}_5\text{C}_2$: A certain portion of precursor PBA-2-3 and thioacetamide (TAA) were dissolved into 64 mL of ethylene glycol and subsequently ultrasonicated for 15 min to yield a homogeneous suspension. Then, the suspension was transferred into a three-neck flask and heating treated in the reaction chamber of a microwave workstation (MCR-3A). Particularly, the heating power, target temperature, heating duration were 500 W, 160 °C and 2 h, respectively. The dark gray product was collected by centrifugation and freeze-dried overnight. Afterwards, the obtained dark gray powder was annealed

in a tube furnace for 2 h at 600 °C in an inert atmosphere, and the final product was characterized as $\text{Co}_8\text{FeS}_8\text{-Fe}_5\text{C}_2$, $\text{Co}_8\text{FeS}_8\text{-Co}_{1-x}\text{S}$, Co_8FeS_8 , and Co_{1-x}S were synthesized by the same condition as that of $\text{Co}_8\text{FeS}_8\text{-Fe}_5\text{C}_2$ but only with PBA-1-3, PBA, and ZIF as precursor, respectively. The detailed information of as-prepared precursors and catalysts in this work were listed in Table S1.

Preparation of $\text{Fe}_3\text{C}@C$: 25 mmol zinc nitrate hexahydrate was dissolved in 500 mL DI water to form solution A. Meanwhile, 12.5 mmol potassium ferricyanide were dissolved in DI water (500 mL) to prepare solution B. Afterwards, the two-solutions were mixed with vigorous stirring and aged for 480 min. The precipitate was collected by centrifugation with a mixture of ethanol and DI water, and subsequently freeze-dried overnight as the prussian blue analogue precursor (Zn-Fe-PBA). Then, the obtained Zn-Fe-PBA was annealed in a quartz tube for 120 min at 800 °C under argon atmosphere.

2.2. Characterization

Powder XRD pattern was recorded on X-ray diffractometer (Japan Rigaku D/MAX-rA) by Cu K α radiation ($\lambda = 1.5418 \text{ \AA}$). Raman spectra were conducted with a Raman spectrometer (Renishaw with the excitation laser wavenumber of 532 nm). SEM tests were characterized using GeminiSEM 300. TEM and HAADF-STEM and EDX mapping were performed on FEI Talos F200x. The spherical aberration-corrected TEM were conducted on Thermo Fisher Scientific Spectra 300 S/TEM. XPS measurements were performed on a model of ESCALAB 250Xi by Al Ka radiation ($h\nu = 1486.6 \text{ eV}$). Inductively coupled plasma-optical emission spectrometer was conducted on Agilent ICP-OES730. The nitrogen adsorption-desorption were performed on ASAP 2460. The electrical conductivity was characterized on a powder resistivity tester (ST-2722). X-ray absorption fine structure spectra (XAFS) of Fe and Co K-edge were collected at BL07A beamline of National Synchrotron Radiation Research Center. The data were collected in fluorescence mode using a Lytle detector. UV-vis diffuse reflection spectroscopy (DRS) on Shimadzu UV-3600 spectrophotometer using BaSO_4 as reference standard. Photoluminescence (PL) emission measurements were carried out by a QuantaMaster™ 40 with an excitation wavelength of 420 nm.

2.3. Electrochemical testing

The electrochemical tests were performed by a standard three-electrode system connected with electrochemical workstation. As-prepared GC electrodes coated with catalyst, graphite rod and Hg/HgO electrode were employed as the working electrode, counter electrode and reference electrode, respectively. The potential conversion between $E_{(\text{Hg}/\text{HgO})}$ and reversible hydrogen electrode ($E_{(\text{RHE})}$) follows $E_{(\text{RHE})} = E_{(\text{Hg}/\text{HgO})} + 0.059 \cdot \text{pH} + 0.098 \text{ V}$. The polarization curves were measured by a linear sweep voltammetry (LSV) approach with a sweeping rate of $1 \text{ mV} \cdot \text{s}^{-1}$ in oxygen- and nitrogen-saturated 1 M KOH solution at ambient temperature. The double-layer capacitance (C_{dl}) was evaluated by cyclic voltammetry (CV) curves performed at the non-faraday reaction regions with an interval of $40 \text{ mV} \cdot \text{s}^{-1}$ over the scanning range of $40\text{--}200 \text{ mV} \cdot \text{s}^{-1}$. EIS was conducted within the frequency range from 0.1 Hz to 100 kHz. The Faradaic efficiency (FE) for OER was analyzed by rotating ring disk electrode according to the following equation:

$$\text{FE} = I_{\text{ring}} / (C_e * I_{\text{disk}})$$

Where I_{disk} and I_{ring} are the pre-set current on disk electrode and detected current on Pt ring, respectively. C_e is the oxygen collection efficient (37 %) for the configuration of used electrode. The ring potential was held at a constant potential of 0.4 V vs RHE in the nitrogen-saturated 0.1 M KOH with a rotation rate of 1600 rpm. The cycling stability was evaluated by the continuous CV technology, and the long-term durability was investigated by the chronoamperometry,

chronopotentiometry.

3. Results and discussion

3.1. Structure, composition, and morphology

Fig. 1a schematically illustrates the synthetic process of $\text{Co}_8\text{FeS}_8\text{-Fe}_5\text{C}_2$ @C. First, cubic-like prussian blue analogue (PBA) precursor was synthesized by a facile coprecipitation reaction between organic ligands (ferricyanogen and dimethyl imidazole) and cobalt ions (XRD pattern and SEM image, Supplementary Figs. 1 and 2). Subsequently, in-situ sulfur adsorption with the assistance of microwave radiation rapid heating process was adopted to convert precursor PBA to intermediate PBA@S with rougher surfaces (XRD pattern and SEM image, Supplementary Figs. 3 and 4). Then, pyrolysis at elevated temperature accompanied by the cleavage of precursor skeleton and sulfidation of metal species, the intermediate PBA@S incubated to be core-shell catalyst with heterostructure $\text{Co}_8\text{FeS}_8\text{-Fe}_5\text{C}_2$ encapsulated in amorphous carbon layers (denoted as $\text{Co}_8\text{FeS}_8\text{-Fe}_5\text{C}_2$ @C).

As exhibited in the transmission electron microscopy image (Fig. 1b and Supplementary Fig. 5), the thickness of carbon shells for $\text{Co}_8\text{FeS}_8\text{-Fe}_5\text{C}_2$ @C is about 4 nm. Fig. 1d and e present the fast Fourier transform (FFT) images viewed from [200] and [021] direction of the Co_8FeS_8 and Fe_5C_2 region, respectively. The hetero-interface can also be definitely observed in the spherical aberration-corrected TEM images (Fig. 1f-h) and the corresponding false-color enhanced images (Fig. 1i and Supplementary Fig. S6). Moreover, the core configuration composed of Co_8FeS_8 and Fe_5C_2 nanocrystals was further revealed by the intensity profiles (Fig. 1j and k), in which the lattice spacing of 2.3 Å and 2.1 Å could be indexed as the Co_8FeS_8 (331) plane and Fe_5C_2 (021) plane [16, 18]. Meanwhile, the uniformly distributed C, N, Co, Fe, and S in the energy dispersive X-ray elemental mapping distributions (Fig. 1L) and the line scanning profiles (Supplementary Fig. S7) evidently supported the formation of core-shell carbon layers coated $\text{Co}_8\text{FeS}_8\text{-Fe}_5\text{C}_2$. Parallelly, control samples of $\text{Co}_8\text{FeS}_8\text{-Co}_{1-x}\text{S}$ @C, Co_8FeS_8 @C, and Co_{1-x}S @C are also prepared to disclose the essence of catalytic kinetic enhancement on the heterointerface engineering level. And their microstructure were scrupulously characterized by high resolution transmission electron microscopy and the detailed results were provided in Supplementary Fig. 8-10.

The crystallinity of the Co_8FeS_8 @C, $\text{Co}_8\text{FeS}_8\text{-Fe}_5\text{C}_2$ @C, $\text{Co}_8\text{FeS}_8\text{-Co}_{1-x}\text{S}$ @C and Co_{1-x}S @C were verified by XRD (Fig. 2a) with the availability of different crystalline phases relating to Co_8FeS_8 (JCPDS card No. 29-0484), Fe_5C_2 (JCPDS card No. 20-0508), and Co_{1-x}S (JCPDS card No. 42-0826) [17,19,20]. It should be noted that the band width of characteristic diffraction peaks of Co_8FeS_8 has the broad trend when the heterostructure is forming. Significantly, miscellaneous peaks were hardly observed in the XRD patterns, testifying the high purity and crystallinity of the as-prepared $\text{Co}_8\text{FeS}_8\text{-Fe}_5\text{C}_2$ and $\text{Co}_8\text{FeS}_8\text{-Co}_{1-x}\text{S}$ heterostructure. Moreover, the Raman spectrum was further conducted to confirm the chemical constitution of the four research samples. As depicted in Fig. 2b, the broad band located at 654.5 cm^{-1} and 443.1 cm^{-1} in the spectra of Co_8FeS_8 @C, $\text{Co}_8\text{FeS}_8\text{-Fe}_5\text{C}_2$ @C, and $\text{Co}_8\text{FeS}_8\text{-Co}_{1-x}\text{S}$ @C arise from the Co-S/Fe-S asymmetric stretching and vibration for Co_8FeS_8 [21]. The prominent bands centered at 285.9 cm^{-1} and 326.1 cm^{-1} could be identified as in-plane (E_{2g}) and out-of-plane (A_{1g}) phonon mode for Fe_5C_2 and Co_{1-x}S , respectively [22-24].

The percentage of Co, Fe, and S are determined in Co_8FeS_8 @C, $\text{Co}_8\text{FeS}_8\text{-Fe}_5\text{C}_2$ @C, $\text{Co}_8\text{FeS}_8\text{-Co}_{1-x}\text{S}$ @C, and Co_{1-x}S @C (Fig. 2c and Supplementary Fig. 11), as ascertained by inductively coupled plasma mass spectrometry. Correspondingly, the molecular ratios of Co_8FeS_8 and Fe_5C_2 in $\text{Co}_8\text{FeS}_8\text{-Fe}_5\text{C}_2$ @C are calculated to be 1:1.95, and the value of Co_8FeS_8 and Co_{1-x}S in $\text{Co}_8\text{FeS}_8\text{-Co}_{1-x}\text{S}$ @C is determined to be 1:4.99. Further based on the TG-DTG analysis (Supplementary Fig. 12), the mass content of coated carbon layer from the combustion process at

the range of 400–700 °C, that is 5.63 %, 3.65 %, 3.15 %, and 0.67 % in Co_{1-x}S @C, Co_8FeS_8 @C, $\text{Co}_8\text{FeS}_8\text{-Co}_{1-x}\text{S}$ @C, and $\text{Co}_8\text{FeS}_8\text{-Fe}_5\text{C}_2$ @C, respectively.

In order to deeply elucidate the existence of strong interaction and charge redistribution at the heterointerfaces between Co_8FeS_8 and Fe_5C_2 (Co_{1-x}S), XPS valence-band measurements, UV-vis diffusive reflectance spectroscopy, and Mott-Schottky plots were performed. As depicted in Supplementary Fig. 13, the x-intercept of Mott-Schottky plots present a flat band potential (E_f) of 0.22, 0.28, and 0.25 V vs. RHE (-8.00, -7.94 and -7.97 eV vs. vacuum level) for Co_8FeS_8 @C, $\text{Co}_8\text{FeS}_8\text{-Fe}_5\text{C}_2$ @C, and $\text{Co}_8\text{FeS}_8\text{-Co}_{1-x}\text{S}$ @C, respectively. The higher E_f energy level of $\text{Co}_8\text{FeS}_8\text{-Fe}_5\text{C}_2$ @C and $\text{Co}_8\text{FeS}_8\text{-Co}_{1-x}\text{S}$ @C meaning a weaker electron binding capacity existed in the heterogeneous interface structure, which would promote more electrons to escape from the catalyst surface sites for catalytic reactions with intermediates [25,26]. The Tauc plots of $(\text{d}h\nu)/2$ versus $h\nu$ derived from UV-vis DRS results (Supplementary Fig. 14) were employed to estimate the band-gap (E_g) of Co_8FeS_8 @C, $\text{Co}_8\text{FeS}_8\text{-Fe}_5\text{C}_2$ @C, and $\text{Co}_8\text{FeS}_8\text{-Co}_{1-x}\text{S}$ @C. Furthermore, Since the prepared samples shows the properties characterized by semiconductors from the results of four-probe electrical resistivity measurement (Supplementary Fig. S15), photoluminescence spectra (Supplementary Fig. S16a), and time-resolve photoluminescence spectra (Supplementary Fig. S16b), the detailed analysis was shown in supplementary materials. Accordingly, the E_g are determined to be 1.71, 1.52, and 1.68 eV (Fig. 2e), respectively, in the light of the Kubelka-Munk remission function [27]. Moreover, the valence band maximum values are calculated to be 0.53 eV, 0.25 eV, and 0.44 eV for Co_8FeS_8 @C, $\text{Co}_8\text{FeS}_8\text{-Fe}_5\text{C}_2$ @C, and $\text{Co}_8\text{FeS}_8\text{-Co}_{1-x}\text{S}$ @C, respectively (Fig. 2d). Obviously, the valence band of Co_8FeS_8 upwards to the Fermi level (E_f) since heterogeneous interface is formed. Given the valence electrons near E_f primarily contribute the d band states, the prominent upshift of the valence band in heterostructure catalyst confirms the shift of E_d energy level [28,29]. Accordingly, the corresponding energy level diagrams were constructed based on the above series of characterization results, as depicted in Fig. 2f. Upon forming Co_8FeS_8 -based heterostructure, the self-driven electron transfer from the Fe_5C_2 and Co_{1-x}S to Co_8FeS_8 could induce the imbalanced distribution and rearrangement of the local charge around the heterointerfaces, which consequently endows the surface of Co_8FeS_8 with the electrophilic region, while the surface of Fe_5C_2 and Co_{1-x}S is nucleophilic.

Since the oxygen catalysis is heavily relied on the types of N moieties due to its electron donating effect of lone pair electrons on enhancing the electrical conductivity of the carbon species. The heteroatom N doped carbon can be evidenced by the deconvoluted peaks from C 1s and N 1s XPS spectra provided in Fig. 2g and h. And the N contents and chemical forms of Co_8FeS_8 @C, $\text{Co}_8\text{FeS}_8\text{-Fe}_5\text{C}_2$ @C, and $\text{Co}_8\text{FeS}_8\text{-Co}_{1-x}\text{S}$ @C are summarized in Fig. 2i. It reveals that $\text{Co}_8\text{FeS}_8\text{-Fe}_5\text{C}_2$ @C contains the highest pyrrolic-N (33.3 %) among the investigated samples, implying that the simultaneous introduction of Fe can increase the percentage of pyrrolic-N. And it is also the possible major reason for its highest content of graphitic-N (29.5 %) due to the direct transformation between pyrrolic and graphitic species at elevated temperatures above 500 °C [30].

To accurately confirm the abovementioned electron transfer behavior from Fe_5C_2 (Co_{1-x}S) to Co_8FeS_8 at phase interfaces in Co_8FeS_8 -based catalysts, high-resolution XPS spectra, synchrotron X-ray absorption near edge structure (XANES) and extended X-ray absorption fine structure (EXAFS) of Co_8FeS_8 @C, $\text{Co}_8\text{FeS}_8\text{-Co}_{1-x}\text{S}$ @C, $\text{Co}_8\text{FeS}_8\text{-Fe}_5\text{C}_2$ @C along with corresponding metal foil (Co foil/Fe foil) and oxides (CoO/Fe₂O₃) as control samples were further investigated. Above all, six prominent peaks can be deconvoluted in core-level Co 2p spectra, which are associated with the Co-S, $\text{Co}^{2+}/\text{Co}^{3+}$, and the satellite peaks, respectively [31]. Especially, the binding energies of Co-S in bimetallic sulfides displays consistently negative shifts of 0.31 compared to that of Co_{1-x}S @C, manifesting the Co possess the tendency to accept electrons from iron species due to the occupation of valence electron for cobalt ion (II) is $3d^7(t_2^5g^2e_g^2)$, in which the t_{2g} orbitals occupancy is characterized

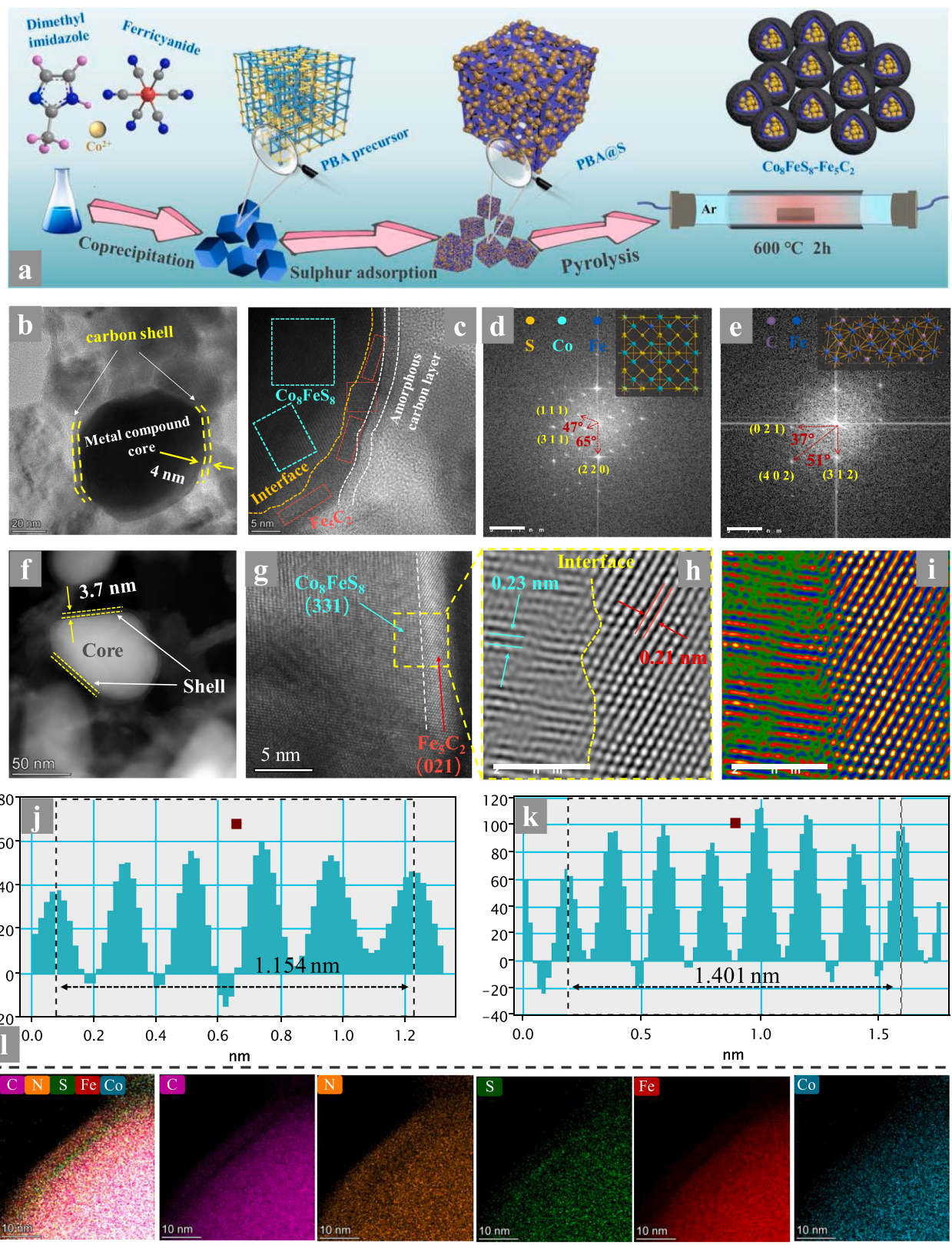


Fig. 1. Schematic representation of synthesis and morphological characterizations. **a** Synthesis illustration, **b**, **c** TEM images, **d**, **e** FFT images, **f**–**i** Spherical aberration-corrected TEM images, **j**–**k** line scanning profiles of the regions marked with cyan and red in **h**, **l** corresponding elemental mappings of carbon, nitrogen, sulfur, iron, and cobalt in Co₈FeS₈–Fe₅C₂ @C.

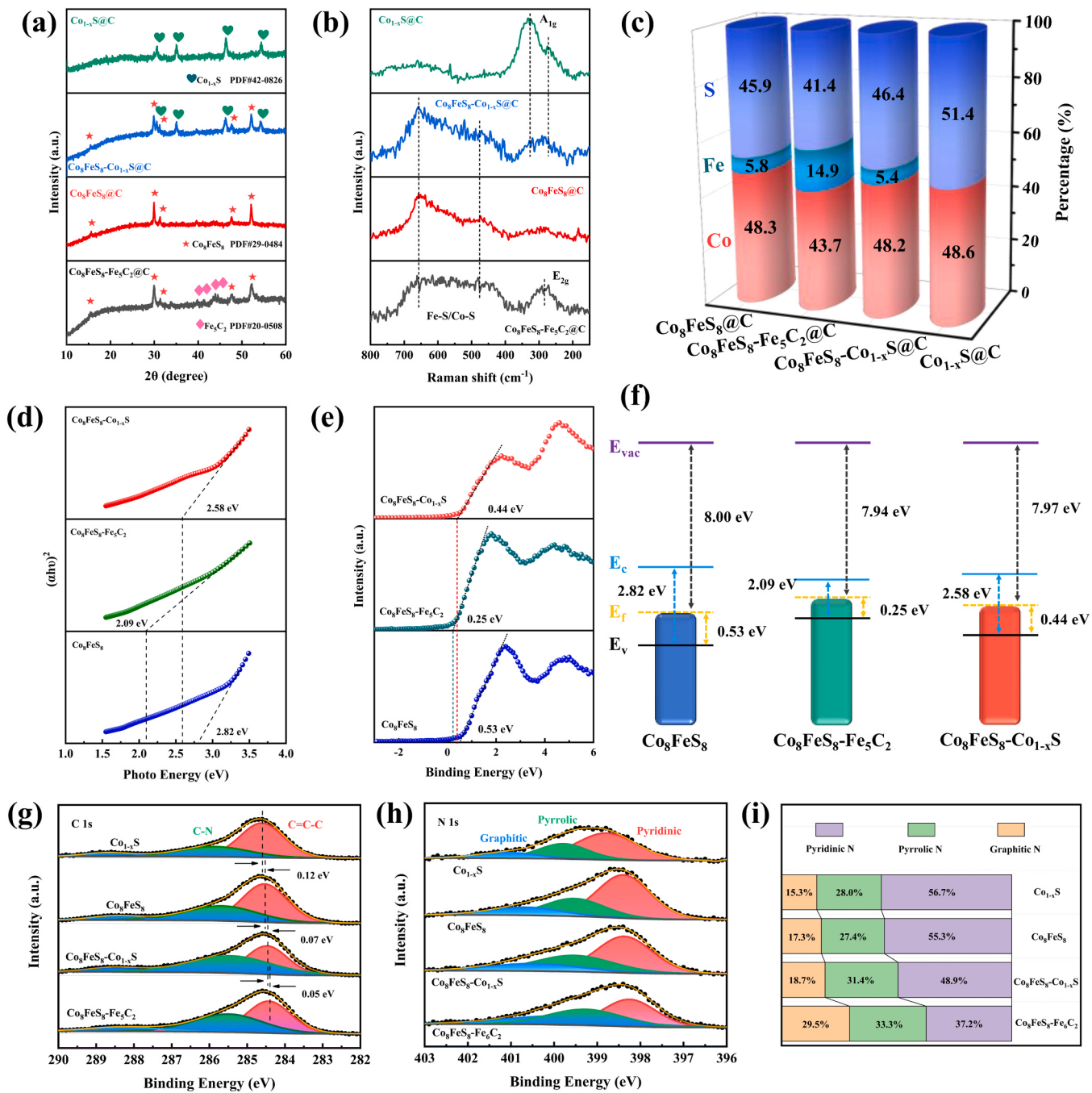


Fig. 2. **a** XRD patterns, **b** Raman spectra, **c** element percentage from ICP-MS analysis of $\text{Co}_8\text{FeS}_8\text{-Fe}_5\text{C}_2$ @C, $\text{Co}_8\text{FeS}_8\text{-Co}_{1-x}\text{S}$ @C, Co_8FeS_8 @C and Co_{1-x}S @C. **d** Plots of $(\alpha h\nu)^2$ versus $h\nu$, **e** valence band XPS spectra, **f** band structure diagram of $\text{Co}_8\text{FeS}_8\text{-Fe}_5\text{C}_2$ @C, $\text{Co}_8\text{FeS}_8\text{-Co}_{1-x}\text{S}$ @C, Co_8FeS_8 @C. **g** high-resolution C 1s and N 1s XPS spectra, **h** N contents and chemical forms, **i** electrical conductivity of the $\text{Co}_8\text{FeS}_8\text{-Fe}_5\text{C}_2$ @C, $\text{Co}_8\text{FeS}_8\text{-Co}_{1-x}\text{S}$ @C, Co_8FeS_8 @C and Co_{1-x}S @C.

with unpaired electron [32,33]. While, the comparison of high-resolution Fe 2p spectra of Co_8FeS_8 based catalysts shows that the iron species in $\text{Co}_8\text{FeS}_8\text{-Fe}_5\text{C}_2$ @C and Co_8FeS_8 @ Co_{1-x}S @C display the diametrically opposite electronic effects, with a pronounced binding energy ($\text{Fe}^{2+}/\text{Fe}^{3+}$) upward and downward shift of 0.19 eV and 0.17 eV, respectively [34]. Obviously, the electron-repulsion effect is dominated for iron species in $\text{Co}_8\text{FeS}_8\text{-Fe}_5\text{C}_2$ @C, while that in Co_8FeS_8 @ Co_{1-x}S @C is electron-attraction effect. Further comparison of the high-resolution S 2p XPS spectra (Supplementary Fig. 17) shows that the S element in $\text{Co}_8\text{FeS}_8\text{-Fe}_5\text{C}_2$ @NC exhibits a relatively stronger electron absorbing property, while a relatively stronger electron repulsive property was in Co_8FeS_8 @ Co_{1-x}S @C.

The Co K-edge XANES spectrum (Fig. 3c) shown that both the pre-edge and white line intensity of Co_8FeS_8 @C, $\text{Co}_8\text{FeS}_8\text{-Co}_{1-x}\text{S}$ @C, and $\text{Co}_8\text{FeS}_8\text{-Fe}_5\text{C}_2$ @C are between Co foil and CoO, suggesting the valence state of Co in the heterostructure is between 0 and +2. In addition, the pre-edge for both $\text{Co}_8\text{FeS}_8\text{-Co}_{1-x}\text{S}$ @C and $\text{Co}_8\text{FeS}_8\text{-Fe}_5\text{C}_2$ @C shift toward higher energy and their white line intensity increase compared with those of Co_8FeS_8 @C counterpart, manifesting the strong electronic interactions between the abundant interface of Co_8FeS_8 and Fe_5C_2 (Co_{1-x}S), as well as a lower electron density at the Co site [35]. Furthermore, in contrast to $\text{Co}_8\text{FeS}_8\text{-Co}_{1-x}\text{S}$ @C, the more positively shift of pre-edge and significantly increase of white line intensity exhibited in $\text{Co}_8\text{FeS}_8\text{-Fe}_5\text{C}_2$ @C confirming the heterogeneous interface between

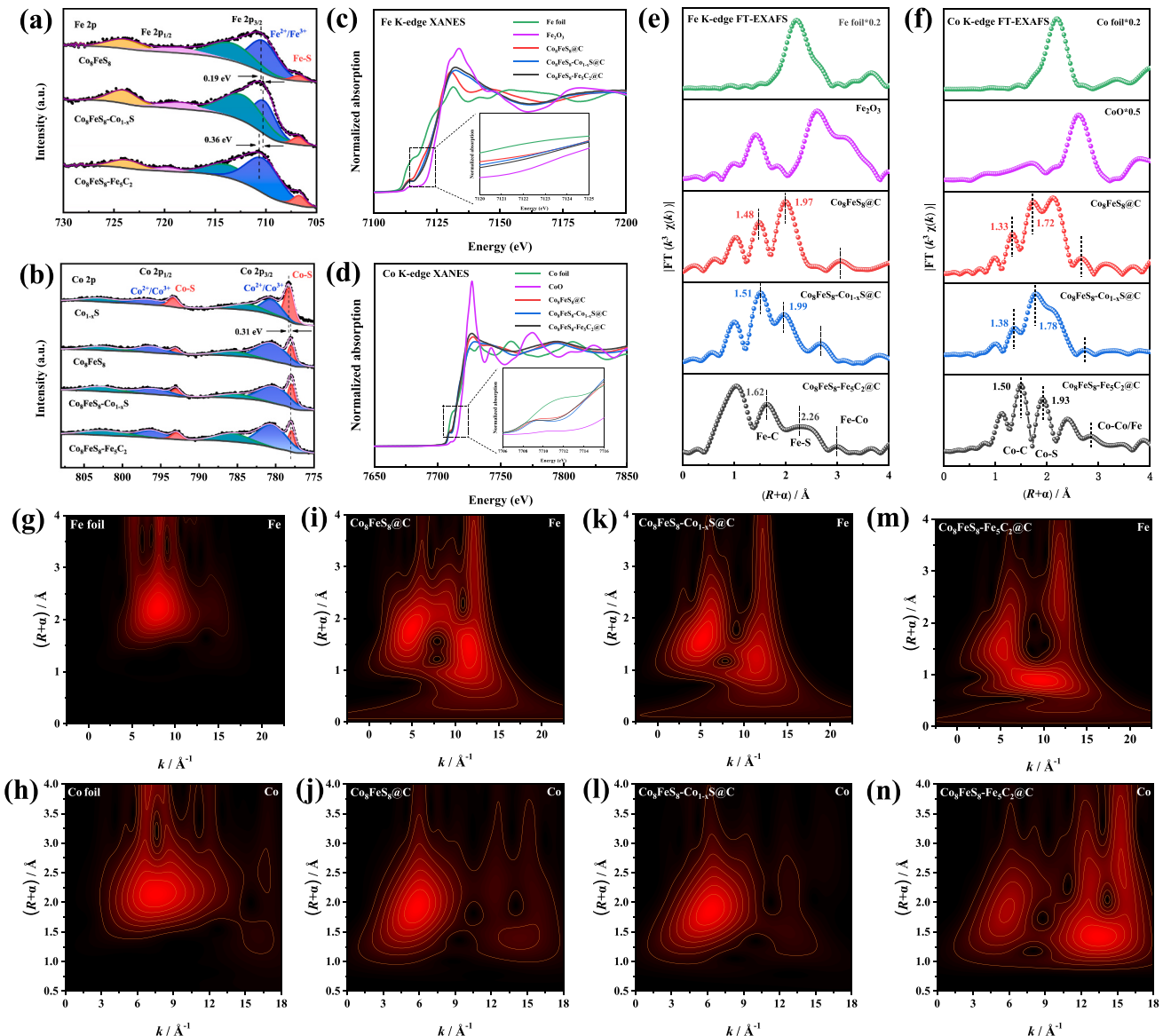


Fig. 3. Electronic states of atoms in electrocatalysts. **a-b** High-resolution XPS spectra of Fe 2p and Co 2p for $\text{Co}_8\text{Fe}_8\text{-Fe}_5\text{C}_2 @\text{C}$, $\text{Co}_8\text{Fe}_8\text{-Co}_{1-x}\text{S} @\text{C}$, $\text{Co}_8\text{Fe}_8 @\text{C}$, and $\text{Co}_{1-x}\text{S} @\text{C}$. **c-d** Fe K-edge XANES spectra and Co K-edge XANES spectra of $\text{Co}_8\text{Fe}_8\text{-Fe}_5\text{C}_2 @\text{C}$, $\text{Co}_8\text{Fe}_8\text{-Co}_{1-x}\text{S} @\text{C}$, $\text{Co}_8\text{Fe}_8 @\text{C}$, metal oxides and foil. **e-f** Fourier transform of k^3 -weighted Fe K-edge of the EXAFS spectra. **g-n** Wavelet transform for the k^3 -weighted EXAFS spectra of metal foil, $\text{Co}_8\text{Fe}_8\text{-Fe}_5\text{C}_2 @\text{C}$, $\text{Co}_8\text{Fe}_8 @\text{C}$, $\text{Co}_{1-x}\text{S} @\text{C}$, $\text{Co}_8\text{Fe}_8 @\text{C}$.

Co_8FeS_8 and carbide will achieve stronger electron coupling in order to achieve a more significant electron rearrangement effect. The above-mentioned analysis result can also be verified by the Fe K-edge XANES spectrum depicted in Fig. 3d.

The Fourier transform k^3 -weighted Fe K-edge EXAFS spectra is provided in Fig. 3e. Apparently, a prominent signal of Fe-S bond at 1.99 Å can be observed in the $k^3\chi(k)$ oscillation curve (k = wave vector and $\chi(k)$ = oscillation as a function of the photoelectron wavenumber) for the $\text{Co}_8\text{FeS}_8\text{-Co}_{1-x}\text{S}_x\text{@C}$, which is slightly shifted by 0.02 Å compared with $\text{Co}_8\text{FeS}_8\text{@C}$. Notably, the corresponding peak of $\text{Co}_8\text{FeS}_8\text{-Fe}_5\text{C}_2\text{@C}$ significantly shifted by 0.29 Å compared with that of $\text{Co}_8\text{FeS}_8\text{@C}$, again manifesting that the local atomic arrangement and interfacial coupling in the heterostructure of Co_8FeS_8 -carbide is significant than Co_8FeS_8 -sulfide [36,37]. Similar results can also be confirmed by the Co K-edge EXAFS spectrum (Fig. 3f). More importantly, based on the XAFS result of $\text{Fe}_3\text{C}@C$ depicted in Supplementary Fig. 18 (the detailed synthesis information and basic characterization were provided in

experimental section and [Supplementary Figs. 19 and 20](#)), metal–carbon bonding signal (Co–C/Fe–C) can be probed in the FT-EXAFS spectrum of the three samples [38,39], in which their peak position shifted gradually in the order $\text{Co}_8\text{FeS}_8\text{-Fe}_5\text{C}_2 @ \text{C} > \text{Co}_8\text{FeS}_8\text{-Co}_{1-x}\text{S}@ \text{C} > \text{Co}_8\text{FeS}_8 @ \text{C}$. Obviously, the interaction between Co_8FeS_8 -based core species and carbon shell layer can be exactly testified and the extent of this interaction depends heavily on phase composition.

For visual illustrations of Co/Fe coordination information, wavelet transforms (WT) of the k^3 -weighted EXAFS spectra, the presentation of structure conditions in the resolution of R space and K space[40], are depicted in Fig. 3g–m and [Supplementary Fig. 21a](#). In detail, the maximum WT intensity at 1.5–2.1 Å in R space and 4–6 Å in K space is attributed to Fe-S bond in the first coordination shell. The maximum WT intensity at 1.0–1.7 Å in R space and 8–13 Å in K space is ascribed to Fe-C bond, as shown in Fig. 3g–m. Analogously, the coexistence of Co-C and Co-S bonds in Co_8FeS_8 -based catalysts can be observed in the WT Co K-edge FT-EXAFS (Fig. h–n and [Supplementary Fig. 22b](#)). Besides, the

hetero-metal bonding (Co-Fe) can be further probed in $\text{Co}_8\text{FeS}_8\text{-Fe}_5\text{C}_2\text{@C}$, implying the significant interface interaction between Co_8FeS_8 and Fe_5C_2 .

Overall, the conjoint analysis of XPS, XANES and EXAFS solidly confirm the interfacial electron transfer from Fe_5C_2 (Co_{1-x}S) to Co_8FeS_8 , and a maximum electron transfer occurred in the former ($\text{Co}_8\text{FeS}_8\text{-Fe}_5\text{C}_2$) for achieving a higher level of catalytic performance. And the more conclusive confirmation could be further preliminarily drawn in the section of DFT calculation analysis. In addition, the unique microstructure and physical properties of strong interfacial coupling, d band

closer to the Fermi level, more balanced proportion of doped nitrogen species, metal-like conductivity, and the geometric carbon coating effect have been exactly proved. And these characteristics of $\text{Co}_8\text{FeS}_8\text{-Fe}_5\text{C}_2\text{@C}$ could be synergistically beneficial for boosting catalytic activity as well enhancing operational stability.

3.2. Electrocatalytic performance

The glassy carbon electrode with the catalyst load of 0.28 mg cm^{-2} as working electrodes for evaluating OER catalysis performance. The

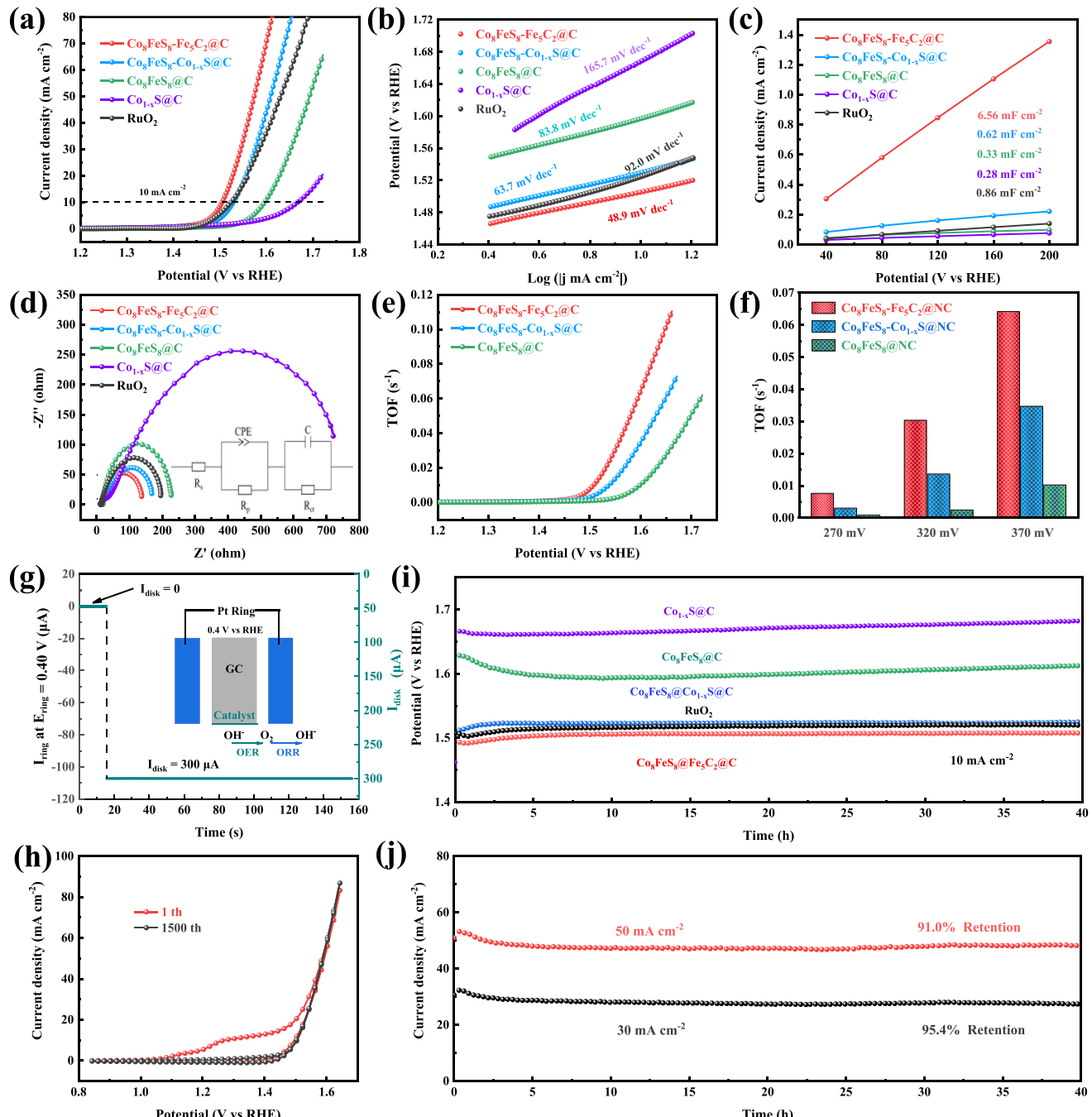


Fig. 4. OER catalytic performance. **a** OER polarization curves, **b** Tafel slopes **c** double-layer capacitances (C_{dl}), **d** charge transfer resistance (R_{ct}), **e** TOF curves and **f** corresponding TOF values under different overpotentials of $\text{Co}_8\text{FeS}_8\text{-Fe}_5\text{C}_2\text{@C}$, $\text{Co}_8\text{FeS}_8\text{-Co}_{1-x}\text{S}@C$, $\text{Co}_8\text{FeS}_8\text{@C}$. **g** Evidence of generated O_2 using rotating ring disk electrode measurement, inset is schematic diagram of testing mechanism. **h** CV curves before and after 1500 cycles, **i** chronopotentiometric tests at 10 mA cm^{-2} of $\text{Co}_8\text{FeS}_8\text{-Fe}_5\text{C}_2\text{@C}$, $\text{Co}_8\text{FeS}_8\text{-Co}_{1-x}\text{S}@C$, $\text{Co}_8\text{FeS}_8\text{@C}$, $\text{Co}_{1-x}\text{S}@C$, and RuO_2 , **j** time-dependent current density curves of $\text{Co}_8\text{FeS}_8\text{-Fe}_5\text{C}_2\text{@C}$.

polarization curves of the electrocatalysts are depicted in Fig. 4a. The target catalyst $\text{Co}_8\text{FeS}_8\text{-Fe}_5\text{C}_2 @\text{C}$ delivers the current densities of 10 mA cm^{-2} with the lowest overpotential ($\eta_{10} = 275 \text{ mV}$) compared with those of $\text{Co}_{1-x}\text{S}@C$ (449 mV), $\text{Co}_8\text{FeS}_8 @C$ (368 mV), and $\text{Co}_8\text{FeS}_8\text{-Co}_{1-x}\text{S}@C$ (301 mV), respectively (Supplementary Fig. 22a). It is worth mentioning that the η_{10} of $\text{Co}_8\text{FeS}_8\text{-Fe}_5\text{C}_2 @\text{C}$ is also smaller than those of benchmark RuO_2 catalyst and Co_8FeS_8 , $\text{Fe-Co}_8\text{S}_8$, Co_8S_8 -based materials (Supplementary Fig. 22b).

To conduct OER kinetic mechanism [41–44], the lowest Tafel slope (Fig. 4b), $48.9 \text{ mV}\cdot\text{dec}^{-1}$ of $\text{Co}_8\text{FeS}_8\text{-Fe}_5\text{C}_2 @\text{C}$ is obtained in comparison of $\text{Co}_{1-x}\text{S}@C$ ($165.7 \text{ mV}\cdot\text{dec}^{-1}$), $\text{Co}_8\text{FeS}_8 @C$ ($83.8 \text{ mV}\cdot\text{dec}^{-1}$), $\text{Co}_8\text{FeS}_8\text{-Co}_{1-x}\text{S}@C$ ($63.7 \text{ mV}\cdot\text{dec}^{-1}$), and RuO_2 ($92.0 \text{ mV}\cdot\text{dec}^{-1}$), indicating the rapid OER kinetics of $\text{Co}_8\text{FeS}_8\text{-Fe}_5\text{C}_2 @\text{C}$ owing to its rapid transfer of electrons at heterointerfaces [45]. Generally, the electrochemically active surface area is considered as an indicator to evaluate the active sites and is proportional to the double-layer capacitance (C_{dl}) [46]. The highest C_{dl} of $\text{Co}_8\text{FeS}_8\text{-Fe}_5\text{C}_2 @\text{C}$ (Fig. 4c and Supplementary Fig. 23) among all samples implies the maximum electroactive area, consistent with its hierarchical porous feature (Supplementary Fig. 24). Moreover, the current of above-mentioned catalysts was normalized to ECSA (Fig. 4f), demonstrating a higher intrinsic activity of $\text{Co}_8\text{FeS}_8\text{-Fe}_5\text{C}_2 @\text{C}$ in comparison of the control group catalysts and commercial RuO_2 . Based on alternating-current impedance technique, $\text{Co}_8\text{FeS}_8\text{-Fe}_5\text{C}_2 @\text{C}$ possesses the lowest charge transfer resistance (R_{ct}) among all tested catalysts (Fig. 4d and Supplementary Fig. 25), confirming a facilitated OER charge transfer kinetics and a fast Faradaic reaction process at the interface between the catalyst and the electrolyte [47].

To illustrate the intrinsic catalytic activity of each active sites for Co_8FeS_8 based catalysts, the turnover frequency (TOF) for $\text{Co}_8\text{FeS}_8\text{-Fe}_5\text{C}_2 @\text{C}$, $\text{Co}_8\text{FeS}_8\text{-Co}_{1-x}\text{S}@C$, and $\text{Co}_8\text{FeS}_8 @C$ were conducted, assuming all metal sites are involved as active sites to quantify the catalytic efficiency [48]. From the TOF curves and corresponding TOF values provided in Fig. 4e and f, the TOF values of $\text{Co}_8\text{FeS}_8\text{-Fe}_5\text{C}_2 @\text{C}$ is $7.6 \times 10^{-3} \text{ s}^{-1}$ at the overpotential of 270 mV, which is ~ 2.5 and ~ 9.4 times higher than that of $\text{Co}_8\text{FeS}_8 @\text{Co}_{1-x}\text{S}@C$ ($3.0 \times 10^{-3} \text{ s}^{-1}$) and $\text{Co}_8\text{FeS}_8 @C$ ($0.8 \times 10^{-3} \text{ s}^{-1}$), respectively. Meanwhile, $\text{Co}_8\text{FeS}_8\text{-Fe}_5\text{C}_2 @\text{C}$ possesses much higher TOF values at the overpotential of 320 mV and 370 mV, implying the highly efficient utilization of metal active sites in heterointerface catalytic system for the electrocatalytic OER process. In addition, the more catalytic active sites stored in $\text{Co}_8\text{FeS}_8\text{-Fe}_5\text{C}_2 @\text{C}$ can also be confirmed by the significantly higher oxidation peak intensity in cyclic voltammetry curve (Supplementary Fig. 26).

To investigate thoroughly the oxidation current in catalytic process was originated exclusively from OER rather than other side reactions, the Faradaic efficiency (FE) was measured by the rotating ring disk electrode technique [49], as schematically depicted in the inset of Fig. 4g. The glassy carbon disk electrode applied with a constant current of $300 \mu\text{A}$ under a rotation speed of 1600 rpm. Meanwhile, Pt ring electrode was held at an oxygen reduction potential of 400 mV vs RHE to detect the generated O_2 from disk electrode. Finally, a current of $109.3 \mu\text{A}$ was detected on the Pt ring electrode and the FE was calculated as 98.4 %, signifying the water oxidation process is not accompanied by secondary reactions in the catalytic process. Meanwhile, the FE of $\text{Co}_8\text{FeS}_8 @\text{Co}_{1-x}\text{S}@C$, $\text{Co}_8\text{FeS}_8 @C$, $\text{Co}_{1-x}\text{S}@C$, and RuO_2 were measured as 98.0 %, 97.4 %, 97.2 %, and 97.7 %, respectively (Supplementary Table 3).

Significantly, the $\text{Co}_8\text{FeS}_8\text{-Fe}_5\text{C}_2 @\text{C}$ shows excellent cycle stability, supported by the almost coincided between the initial and after consecutive 1500th CV curves in the current diffusion region (Fig. 4h). Besides, $\text{Co}_8\text{FeS}_8\text{-Fe}_5\text{C}_2 @\text{C}$ can continuously and stably proceed the OER catalytic process at 10 mA cm^{-2} with the lowest overpotential, evidenced by the time-dependent potential curves (Fig. 4i). Moreover, there is no obvious degradation in the chronoamperometric curves with a initial current density of 30 and 50 mA cm^{-2} (Fig. 4j), and the retention of current density is 95.4 % and 91.0 % after 40 h of OER operation.

The above tests indicate the target $\text{Co}_8\text{FeS}_8\text{-Fe}_5\text{C}_2 @\text{C}$ catalyst possesses qualified OER stability required in practical applications due to the synergistic effect of the carbon coated core-shell configuration.

3.3. Theoretical calculation analysis

For insights into intrinsically OER electrocatalytic activity of $\text{Co}_8\text{FeS}_8\text{-Fe}_5\text{C}_2 @\text{C}$, the density functional theory (DFT) calculations about Gibbs free energies of oxygen-containing intermediates were performed. Theoretically, the underlying mechanism proposed by Nørskov et al. for the water oxidation in alkaline medium is $4\text{OH} \rightarrow 2 \text{H}_2\text{O} + \text{O}_2 + 4e^-$ [50], in which four reaction steps including the adsorption, dissociation and desorption of $^*\text{OH}$, $^*\text{O}$, and $^*\text{OOH}$ intermediates are involved, as schematically depicted in Fig. 5b. On the basis of the above characterization results, the crystal models of $\text{Co}_8\text{FeS}_8 @C$, $\text{Co}_8\text{FeS}_8 @\text{Co}_{1-x}\text{S}@C$, and $\text{Co}_8\text{FeS}_8\text{-Fe}_5\text{C}_2 @C$ are constructed (Fig. 5a and Supplementary Fig. 27). The Co atoms in $\text{Co}_8\text{FeS}_8 @C$, $\text{Co}_8\text{FeS}_8 @\text{Co}_{1-x}\text{S}@C$ and Fe atoms in $\text{Co}_8\text{FeS}_8\text{-Fe}_5\text{C}_2 @C$ are preferentially selected as the active sites on the surface of Co_8FeS_8 (200), and the coupled heterostructure of Co_8FeS_8 (200)/ Co_{1-x}S (102) and Co_8FeS_8 (200)/ Fe_5C_2 (021) when calculating the Gibbs free energy (ΔG). The free energy diagram of OER path at zero potential are summarized in Fig. 5c, and the more detailed calculation process is described in the supplementary materials.

The computational results indicate that all the elementary reaction steps undergo an endothermic process and the formation of $^*\text{OOH}$ from $^*\text{O}$ is definitely identified as the rate-determining step (RDS). Furthermore, the RDS for $\text{Co}_8\text{FeS}_8 @C$ with a larger ΔG of 2.05 eV (Fig. 5d) demonstrates the weak binding strength of OOH^* on the Co_8FeS_8 surface [51]. Obviously, when coupled with Co_{1-x}S and Fe_5C_2 , the ΔG is respectively decreased to be 1.98 eV and 1.81 eV, indicating the construction of heterointerfaces is an efficient strategy to optimize the adsorption energy of oxygen-involving reactants and reduce the thermodynamic potential barrier.

Moreover, the interfacial charge distribution in hybrid system was depicted in Supplementary Fig. 28. From the differential charge density, one can see that charge distribution of $\text{Co}_8\text{FeS}_8 @\text{Co}_{1-x}\text{S}@C$ and $\text{Co}_8\text{FeS}_8\text{-Fe}_5\text{C}_2 @C$ is more polarized at the interface in contrast with that of $\text{Co}_8\text{FeS}_8 @C$. We quantified the charge transfer at the interface by computing the plane-averaged electron density difference of $\text{Co}_8\text{FeS}_8 @C$, $\text{Co}_8\text{FeS}_8 @\text{Co}_{1-x}\text{S}@C$, and $\text{Co}_8\text{FeS}_8\text{-Fe}_5\text{C}_2 @C$ (Supplementary Fig. 29). Then, we notice that the electron transfer from Fe_5C_2 (Co_{1-x}S) inward to Co_8FeS_8 and outward to carbon layer, which is consistent with the previous analysis. Besides, the charge redistribution at the $\text{Co}_8\text{FeS}_8/\text{Fe}_5\text{C}_2$ interface is stronger than that of $\text{Co}_8\text{FeS}_8/\text{Co}_{1-x}\text{S}$, confirming that carbide is effective in reinforcing the interaction between the Co_8FeS_8 and metallic compound. It is worth noting that the density of states for $\text{Co}_8\text{FeS}_8\text{-Fe}_5\text{C}_2 @C$ near the Fermi energy (E_f) is primarily the contribution of d orbital of Fe and s orbital of C, suggesting that Fe_5C_2 is more suitable to be regarded as the main catalytic species in $\text{Co}_8\text{FeS}_8\text{-Fe}_5\text{C}_2 @C$, as depicted in Supplementary Fig. 30.

It is well known that the bonding states far below E_f are fully occupied, while the electron filling of the anti-bonding states depends on their energy states relative to E_f [52,53]. In general, the higher of anti-bonding energy states, the stronger interaction between the reactants and catalyst surface, on the contrary, it weakened. So, the d-band center (ϵ_d) is a reliable descriptor to bridge the anti-bonding energy states with adsorption energy of an adsorbate and thus the OER performance. As shown in Fig. 5e, the ϵ_d of $\text{Co}_8\text{FeS}_8\text{-Fe}_5\text{C}_2 @C$ and $\text{Co}_8\text{FeS}_8\text{-Co}_{1-x}\text{S}@C$ shift upward toward the Fermi level compared with that of $\text{Co}_8\text{FeS}_8 @C$, implying the lower probability of electron filling in antibonding orbital after the formation of Co_8FeS_8 -based heterostructure. Impressively, the upshift of ϵ_d energy level for $\text{Co}_8\text{FeS}_8\text{-Fe}_5\text{C}_2 @C$ is more significant than that of $\text{Co}_8\text{FeS}_8 @\text{Co}_{1-x}\text{S}@C$, indicating the stronger interaction between intermediates and catalytic surface impedes the occurrences of electrocatalytic OER process with a faster

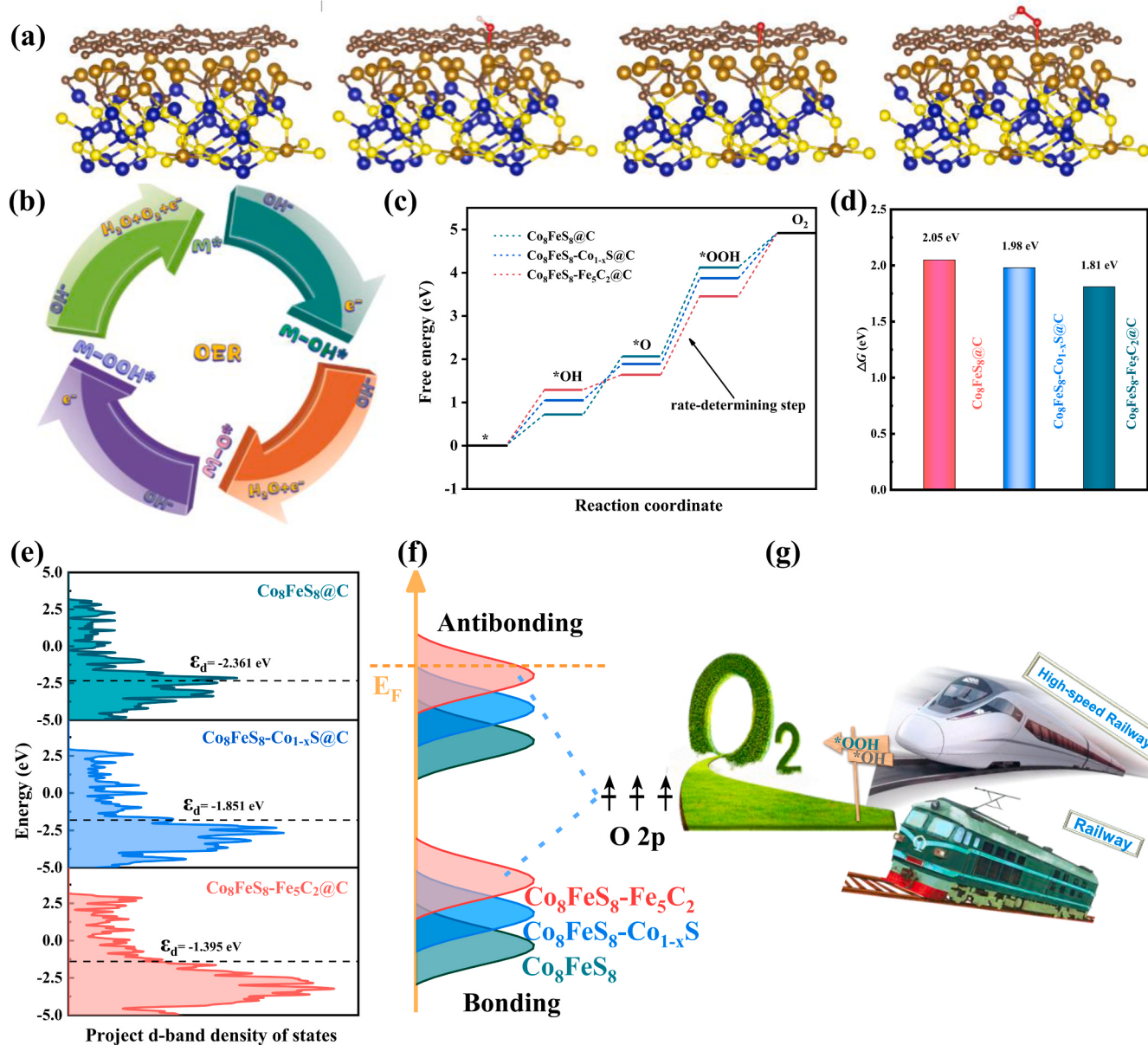


Fig. 5. DFT calculations. **a** Schematic diagram of the elementary reaction steps water oxidation, **b** free-energy diagrams of $\text{Co}_8\text{FeS}_8@\text{C}$, $\text{Co}_8\text{FeS}_8-\text{Co}_{1-x}\text{S}@\text{C}$ and $\text{Co}_8\text{FeS}_8-\text{Fe}_5\text{C}_2@\text{C}$. Inset is OH , O , and OOH intermediates adsorption configurations on $\text{Co}_8\text{FeS}_8-\text{Fe}_5\text{C}_2@\text{C}$. **c** Free energy (eV) vs. reaction coordinate for the OER cycle. **d**, **e**, **f** differential charge densities of **d** $\text{Co}_8\text{FeS}_8@\text{C}$, **e** $\text{Co}_8\text{FeS}_8-\text{Co}_{1-x}\text{S}@\text{C}$, and **f** $\text{Co}_8\text{FeS}_8-\text{Fe}_5\text{C}_2@\text{C}$. The cyan and yellow colors are regions of electron accumulation and depletion, respectively. **g**, **h**, **i** density of states. **j** calculated d-band center, **k** schematic of d-band center elevating of **g** $\text{Co}_8\text{FeS}_8@\text{C}$, **h** $\text{Co}_8\text{FeS}_8-\text{Co}_{1-x}\text{S}@\text{C}$, and **i** $\text{Co}_8\text{FeS}_8-\text{Fe}_5\text{C}_2@\text{C}$, **l** schematic illustration for the enhancement of kinetics in OER process.

kinetic (Fig. 5f). Thus, as illustrated in Fig. 5g, for the highly active OER electrocatalyst, the high-efficiency transformation of intermediates ($^{*}\text{O}$ and $^{*}\text{OOH}$) involving in RDS is the key to significantly reduce the energy barrier and finally enhance the reaction kinetics.

3.4. Electrocatalytic performance for overall water splitting and Zn-Air battery

The $\text{Co}_8\text{FeS}_8-\text{Fe}_5\text{C}_2@\text{C}$ also shows good HER activity: it exhibits an overpotential of 187 mV at 10 mA cm^{-2} for HER (Fig. 6a and supplementary Fig. 31). Inspired by its bifunctional catalytic properties, in a proof-of-principle demonstration of its application for electrochemical energy conversion, herein, we first leveraged the OER+HER activity of $\text{Co}_8\text{FeS}_8-\text{Fe}_5\text{C}_2@\text{C}$ and set up a two-electrode electrolyzer, in which the $\text{Co}_8\text{FeS}_8-\text{Fe}_5\text{C}_2@\text{C}$ supported on iron foam (IF) was assembled as

both anode and cathode (Fig. 6b). The robust catalytic performance was obtained by as-prepared $\text{Co}_8\text{FeS}_8-\text{Fe}_5\text{C}_2@\text{C} \parallel \text{Co}_8\text{FeS}_8-\text{Fe}_5\text{C}_2@\text{C}$ electrode, requiring the low cell voltages of 1.55, 1.65, 1.72, and 1.78 V at 10, 50, 100, and 150 mA cm^{-2} in 1 M KOH under ambient temperature (Fig. 6c and d). Impressively, its performance is superior to that of benchmark Pt/C catalyst at high current density ($> 100 \text{ mA cm}^{-2}$) in water electrolysis, which due to the avoidance of cross contamination from the incompatible combination of two single-function catalysts.

To measure the Faradaic efficiency for water electrolysis, we collected the produced H_2 and O_2 during the overall water splitting by the water drainage method (Fig. 6e). As shown in Fig. 6f, the volume ratio of hydrogen to oxygen is about 2.04:1, approaching the theoretical value (2:1), which manifests its nearly 100 % Faradaic efficiency. Moreover, the $\text{Co}_8\text{FeS}_8-\text{Fe}_5\text{C}_2@\text{C} \parallel \text{Co}_8\text{FeS}_8-\text{Fe}_5\text{C}_2@\text{C}$ pair also displays excellent long-term stability with the almost unattenuated current

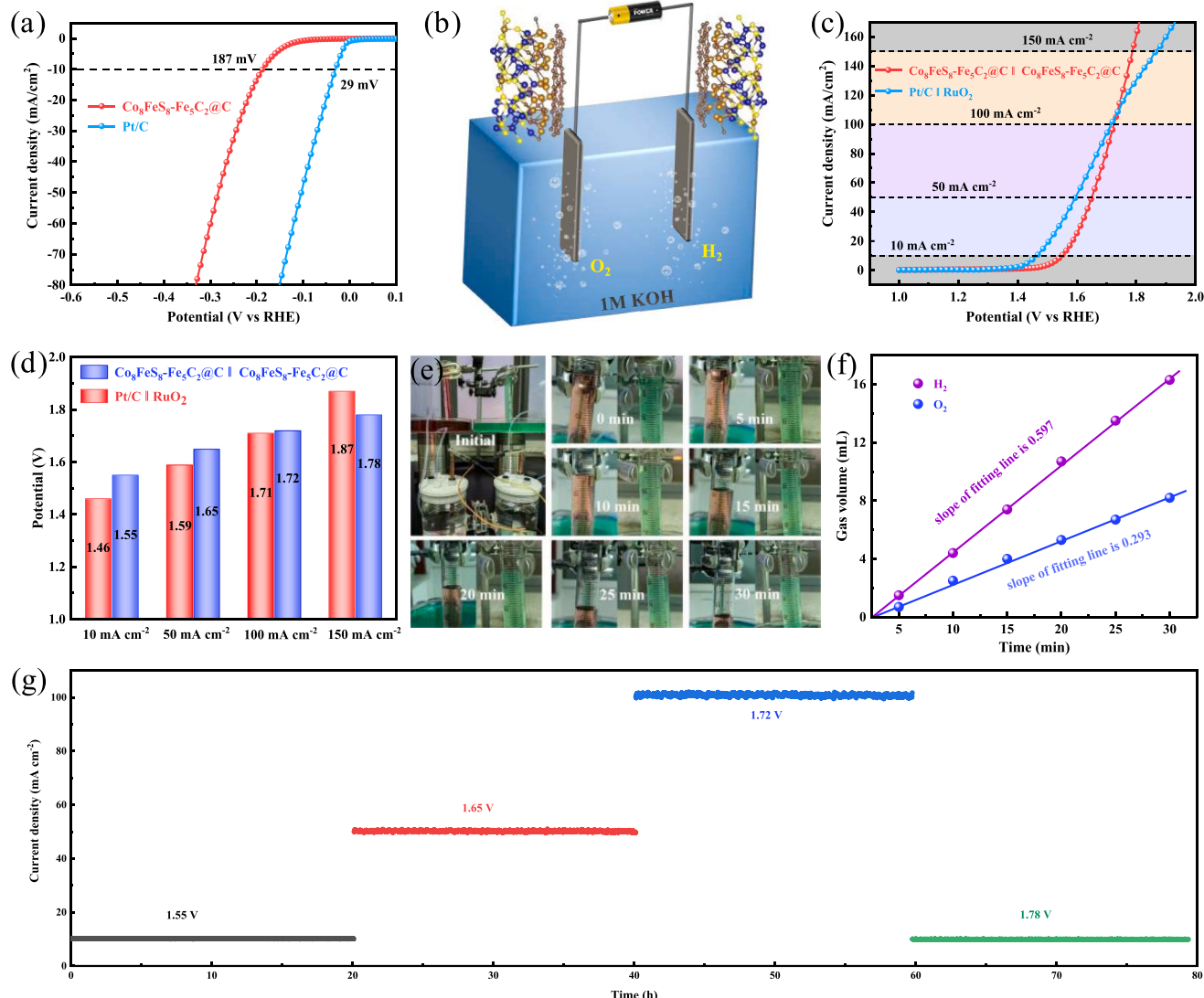


Fig. 6. Electrocatalytic performance for overall water splitting. **a** HER polarization curves, **b** Schematic diagram of water splitting in a two-electrode configuration, **c** polarization curves by two-electrode system, **d** overpotentials at typical current densities, **e** photographs of lab-made gas collectors with 5 min interval, **f** plots of theoretically calculated and experimentally collected oxygen and hydrogen gas vs. time by a water-drainage method, **g** Long-term stability test of $\text{Co}_8\text{FeS}_8\text{-Fe}_5\text{C}_2@C || \text{Co}_8\text{FeS}_8\text{-Fe}_5\text{C}_2@C$ for water splitting at $V = 1.55, 1.65, 1.72$ and 1.78 V for 80 h.

densities after the overall water splitting tests under increased applied voltage, as shown in Fig. 6g.

In addition to its promising electrocatalytic OER performance, $\text{Co}_8\text{FeS}_8\text{-Fe}_5\text{C}_2@C$ also shows good ORR activity: it exhibits a half-wave potential of 0.76 V for ORR (Supplementary Figs. 32). A rechargeable Zn-Air battery was assembled leveraged by its OER+ORR catalytic activity. Supplementary Fig. 33a demonstrates the configuration of the home-made cell device, in which carbon paper integrated with $\text{Co}_8\text{FeS}_8\text{-Fe}_5\text{C}_2@C$, polished Zn plate, and 6 M KOH + 0.2 M $\text{Zn}(\text{Ac})_2$ aqueous solution were employed as the air cathode, anode, and electrolyte, respectively. The counterpart cell device supported by noble metal catalyst (mixture of Pt/C + IrO₂ with a mass ratio of 1: 3) was also assembled for performance comparison. Expectedly, the assembled devices based on $\text{Co}_8\text{FeS}_8\text{-Fe}_5\text{C}_2@C$ displays better performances compared with RuO₂ + Pt/C mixed catalysts (Supplementary Fig. 33b–e). And the detailed analysis and discussion were provided in supplementary materials.

4. Conclusion

In conclusion, we proposed a design principle for a catalyst system with Co_8FeS_8 -based heterostructure confined in carbon layers using a microwave-assisted sulfur adsorption and subsequently annealing technique by use of dual-ligand PBA as the precursor. The enhanced electrocatalytic OER performance of $\text{Co}_8\text{FeS}_8\text{-Fe}_5\text{C}_2@C$ is attributed to the following reasons. (1) rapid electron transfer enabled by the nano configuration with iron carbide as interlayer of carbon coated core-shell catalyst. (2) the coupling interface between Co_8FeS_8 and Fe_5C_2 can significantly elevating d-band center of Co_8FeS_8 to realize stronger adsorption strength for oxygen-involving intermediates. By virtue of its additional catalytic HER and ORR properties, its trifunctional catalytic activities are leveraged to be realized in the application of water electrolysis and rechargeable Zn-Air battery. Expectedly, the assembled devices based on $\text{Co}_8\text{FeS}_8\text{-Fe}_5\text{C}_2@C$ displays better performances compared with precious metal-based catalysts (RuO₂ + Pt/C). We anticipate that this work could provide the reference to the researches on effectively improving the catalytic kinetic property through the modulation of d-band center by interface engineering, and pave the path

towards designing excellent Co_3FeS_8 -based multifunctional electrocatalysts as the most viable alternative to the current precious metal catalysts.

CRediT authorship contribution statement

Bin Wang: Conceptualization, Investigation, Formal analysis, Validation, Data curation, Writing – original draft. **Yuanfu Chen and Renbing Wu:** Conceptualization, Methodology, Writing – review & editing, Project administration, Funding acquisition. **Gu Liu, Dawei Liu and Yanfang Liu:** Visualization, Data curation. **Chaoqun Ge:** Investigation, Validation. **Long Wang:** Writing – review & editing. **Zegao Wang and Liuying Wang:** Supervision, Resources, Project administration.

Declaration of Competing Interest

The authors declare that they have no known competing financial interests or personal relationships that could have appeared to influence the work reported in this paper.

Data Availability

Data will be made available on request.

Acknowledgements

We thank the financial support from the National Natural Science Foundation of China (Grant No. 21773024), Natural Science Basic Research Program of Shaanxi (No. 2022JQ-356), China Postdoctoral Science Foundation (2022M723884), Sichuan Natural Science Foundation Project (Grant No. 23NSFSC0370), Reformation and Development Funds for Local Region Universities from China Government in 2020 (Grant No. ZCKJ 2020-11).

Appendix A. Supporting information

Supplementary data associated with this article can be found in the online version at [doi:10.1016/j.apcatb.2023.123294](https://doi.org/10.1016/j.apcatb.2023.123294).

References

- [1] M.C. Luo, Z.L. Zhao, Y.L. Zhang, PdMo bimetallene for oxygen reduction catalysis, *Nature* 574 (2019) 81–85, <https://doi.org/10.1038/s41586-019-1603-7>.
- [2] W.R. Cheng, X. Zhao, H. Su, Lattice-strained metal-organic-framework arrays for bifunctional oxygen electrocatalysis, *Nat. Energy* 4 (2019) 115–122, <https://doi.org/10.1038/s41560-018-0308-8>.
- [3] Y.N. Guo, T. Park, J.W. Yi, Nanoarchitectonics for transition-metal-sulfide-based electrocatalysts for water splitting, *Adv. Mater.* 31 (2019), e1807134, <https://doi.org/10.1002/adma.201807134>.
- [4] S.S. Li, Y.Q. Gao, N. Li, Transition metal-based bimetallic MOFs and MOF-derived catalysts for electrochemical oxygen evolution reaction, *Energy Environ. Sci.* 14 (2021) 1897–1927, <https://doi.org/10.1039/d0ee03697h>.
- [5] X.B. Zhang, J. Wang, H.X. Zhong, Integrated three-dimensional carbon paper/carbon tubes/cobalt-sulfide sheets as an efficient electrode for overall water splitting, *ACS Nano* 10 (2016) 2342–2348, <https://doi.org/10.1021/acsnano.5b07126>.
- [6] J.Y. Zhang, X.W. Bai, T.T. Wang, Bimetallic nickel cobalt sulfide as efficient electrocatalyst for Zn-Air battery and water splitting, *Nano-Micro Lett.* 11 (2019), 2, <https://doi.org/10.1007/s40820-018-0232-2>.
- [7] S. Dou, L. Tao, J. Huo, Etched and doped Co_3S_8 /graphene hybrid for oxygen electrocatalysis, *Energy Environ. Sci.* 9 (2016) 1320–1326, <https://doi.org/10.1039/c6ee00054a>.
- [8] X. Zhang, S.W. Sheng, Y.P. Zang, Co/ Co_3S_8 @S,N-doped porous graphene sheets derived from S, N dual organic ligands assembled Co-MOFs as superior electrocatalysts for full water splitting in alkaline media, *Nano Energy* 30 (2016) 93–102, <https://doi.org/10.1016/j.nanoen.2016.09.040>.
- [9] M. Wang, Z. Wan, X.Y. Meng, Heterostructured Co/Mo-sulfide catalyst enables unbiased solar water splitting by integration with perovskite solar cells, *Appl. Catal. B-Environ.* 309 (2022), 121272, <https://doi.org/10.1016/j.apcatb.2022.121272>.
- [10] Y. Yang, H.Q. Yao, Z.H. Yu, Hierarchical nanoassembly of $\text{MoS}_2/\text{Co}_3\text{S}_8/\text{Ni}_3\text{S}_2/\text{Ni}$ as a highly efficient wide-pH range electrocatalyst for overall water splitting, *J. Am. Chem. Soc.* (26) (2019) 10417–10430, <https://doi.org/10.1021/jacs.9b04492>.
- [11] S.J. Deng, Y. Zhong, Y.X. Zeng, Hollow $\text{TiO}_2@\text{Co}_3\text{S}_8$ core-branch arrays as bifunctional electrocatalysts for efficient oxygen/hydrogen production, *Adv. Sci.* 5 (2018), 1700772, <https://doi.org/10.1002/advs.201700772>.
- [12] H. Zhu, J.F. Zhang, R.Y. Zhang, When cubic cobalt sulfide meets layered molybdenum disulfide: a core-shell system toward synergistic electrocatalytic water splitting, *Adv. Mater.* 27 (2015) 4752–4759, <https://doi.org/10.1002/adma.201501969>.
- [13] L.G. Wang, X.X. Duan, X.J. Liu, Atomically dispersed Mo supported on metallic Co_3S_8 nanoflakes as an advanced noble-metal-free bifunctional water splitting catalyst working in universal pH conditions, *Adv. Energy Mater.* 10 (2019), 1903137, <https://doi.org/10.1002/aenm.201903137>.
- [14] Q. Shao, J.Q. Liu, Q. Wu, In situ coupling strategy for anchoring monodisperse Co_3S_8 nanoparticles on S and N dual-doped graphene as a bifunctional electrocatalyst for rechargeable Zn-Air battery, *Nano-Micro Lett.* 11 (2019) 2–14, <https://doi.org/10.1007/s40820-018-0231-3>.
- [15] Z.P. Wang, Z.P. Lin, J. Deng, Elevating the d-band center of six-coordinated octahedrons in Co_3S_8 through Fe-incorporated topochemical deintercalation, *Adv. Energy Mater.* 11 (2020), 2003023, <https://doi.org/10.1002/aenm.202003023>.
- [16] B. Wang, Y. Hu, B. Yu, Heterogeneous CoFe- Co_3S_8 nanoparticles embedded in CNT networks as highly efficient and stable electrocatalysts for oxygen evolution reaction, *J. Power Sources* 433 (2019), 126688, <https://doi.org/10.1016/j.jpowsour.2019.05.094>.
- [17] B. Wang, Y.F. Wang, X.Q. Wang, A microwave-assisted bubble bursting strategy to grow $\text{Co}_3\text{FeS}_8/\text{CoS}$ heterostructure on rearranged carbon nanotubes as efficient electrocatalyst for oxygen evolution reaction, *J. Power Sources* 449 (2020), 227561, <https://doi.org/10.1016/j.jpowsour.2019.227561>.
- [18] E.L. Hu, X.Y. Yu, F. Chen, Graphene layers-wrapped Fe/ Fe_3C_2 nanoparticles supported on N-doped graphene nanosheets for highly efficient oxygen reduction, *Adv. Energy Mater.* 8 (2018), 1702476, <https://doi.org/10.1002/aenm.201702476>.
- [19] B. Zhao, P. Zhai, P.F. Wang, Direct transformation of syngas to aromatics over Na-Zn- Fe_3C_2 and hierarchical HZSM-5 tandem catalysts, *Chemistry* 3 (2017) 323–333, <https://doi.org/10.1016/j.chempr.2017.06.017>.
- [20] X.J. Zhang, J.Q. Zhu, P.G. Yin, Tunable high-performance microwave absorption of Co_{1-x}S hollow spheres constructed by nanosheets within ultralow filler loading, *Adv. Funct. Mater.* 28 (2018), 1800761, <https://doi.org/10.1002/adfm.201800761>.
- [21] Z.Y. Gao, C. Chen, J.L. Chang, Porous $\text{Co}_3\text{S}_4@\text{Ni}_3\text{S}_4$ heterostructure arrays electrode with vertical electrons and ions channels for efficient hybrid supercapacitor, *Chem. Eng. J.* 343 (2018) 572–582, <https://doi.org/10.1016/j.cej.2018.03.042>.
- [22] J.F. Lin, O. Pitkanen, J. Maklin, Synthesis of tungsten carbide and tungsten disulfide on vertically aligned multi-walled carbon nanotube forests and their application as non-Pt electrocatalysts for the hydrogen evolution reaction, *J. Mater. Chem. A* 3 (2015) 14609–14616, <https://doi.org/10.1039/c5ta02908b>.
- [23] C. Yang, H.B. Zhao, Y.L. Hou, Fe_3C_2 nanoparticles: a facile bromide-induced synthesis and as an active phase for Fischer-Tropsch synthesis, *J. Am. Chem. Soc.* 134 (2012) 15814–15821, <https://doi.org/10.1021/ja305048p>.
- [24] Y.W. Li, W. Gao, M. Peng, Interfacial $\text{Fe}_3\text{C}_2\text{-Cu}$ catalysts toward low-pressure syngas conversion to long-chain alcohols, *Nat. Commun.* 11 (2020), 61, <https://doi.org/10.1038/s41467-019-13691-4>.
- [25] S. Ni, H.G. Qu, Z.H. Xu, Interfacial engineering of the $\text{NiSe}_2/\text{FeSe}_2$ p-p heterojunction for promoting oxygen evolution reaction and electrocatalytic urea oxidation, *Appl. Catal. B-Environ.* 299 (2021), 120638, <https://doi.org/10.1016/j.apcatb.2021.120638>.
- [26] Z.H. Liu, H. Tan, D.B. Liu, Promotion of overall water splitting activity over a wide pH range by interfacial electrical effects of metallic NiCo-nitrides nanoparticle/ NiCo_2O_4 nanoflake/graphite fibers, *Adv. Sci.* 6 (2019), 1801829, <https://doi.org/10.1002/advs.201801829>.
- [27] J.Q. Sun, S.E. Lowe, L.J. Zhang, Ultrathin nitrogen-doped holey carbon@graphene bifunctional electrocatalyst for oxygen reduction and evolution reactions in alkaline and acidic media, *Angew. Chem. Int. Ed.* 57 (2018) 16511–16515, <https://doi.org/10.1002/anie.201811573>.
- [28] S.F. Sun, X. Zhou, B.W. Cong, Tailoring the d-band centers endows ($\text{Ni}_x\text{Fe}_{1-x}\text{S}_2\text{P}$) nanosheets with efficient oxygen evolution catalysis, *ACS Catal.* 10 (2020) 9086–9097, <https://doi.org/10.1021/acscatal.0c01273>.
- [29] C.F. Li, J.W. Zhao, L.J. Xie, Surface-adsorbed carboxylate ligands on layered double hydroxides/metal-organic frameworks promote the electrocatalytic oxygen evolution reaction, *Angew. Chem. Int. Ed.* 60 (2021) 18129–18137, <https://doi.org/10.1002/anie.202104148>.
- [30] T. Ouyang, Y.Q. Ye, C.Y. Wu, Heterostructures composed of N-doped carbon nanotubes encapsulating cobalt and beta- Mo_2C nanoparticles as bifunctional electrodes for water splitting, *Angew. Chem. Int. Ed.* 58 (2019) 4923–4928, <https://doi.org/10.1002/anie.201814262>.
- [31] J. Yang, G.X. Zhu, Y.J. Liu, Fe_3O_4 -decorated Co_3S_8 nanoparticles in situ grown on reduced graphene oxide: a new and efficient electrocatalyst for oxygen evolution reaction, *Adv. Adv. Funct. Mater.* 26 (2016) 4712–4721, <https://doi.org/10.1002/adfm.201600674>.
- [32] Y.G. Zhao, N.C. Dongfang, C.A. Triana, Dynamics and control of active sites in hierarchically nanostructured cobalt phosphide/chalcogenide-based electrocatalysts for water splitting, *Energy Environ. Sci.* 15 (2022) 727–739, <https://doi.org/10.1039/dlee02249k>.

[33] T.Z. Wu, S.G. Sun, J.J. Song, Iron-facilitated dynamic active-site generation on spinel CoAl_2O_4 with self-termination of surface reconstruction for water oxidation, *Nat. Catal.* 2 (2019) 763–772, <https://doi.org/10.1038/s41929-019-0325-4>.

[34] Z.Y. He, J. Zhang, Z.H. Gong, Activating lattice oxygen in NiFe-based (oxy) hydroxide for water electrolysis, *Nat. Commun.* 13 (2022), 2191, <https://doi.org/10.1038/s41467-022-29875-4>.

[35] H. Liu, J.N. Cheng, W.J. He, Interfacial electronic modulation of Ni_3S_2 nanosheet arrays decorated with Au nanoparticles boosts overall water splitting, *Appl. Catal. B-Environ.* 304 (2022), 120935, <https://doi.org/10.1016/j.apcatb.2021.120935>.

[36] W.Q. Yao, W.Z. Zeng, J. X, ZnS-SnS@NC heterostructure as robust lithiophilicity and sulphophilicity mediator toward high-rate and long-life lithium-sulfur batteries, *ACS Nano* 15 (2021) 7114–7130, <https://doi.org/10.1021/acsnano.1c00270>.

[37] Q. Zhang, J.H. Zhang, X.H. Wang, In-N-In sites boosting interfacial charge transfer in carbon-coated hollow tubular $\text{In}_2\text{O}_3/\text{ZnIn}_2\text{S}_4$ heterostructure derived from In-MOF for enhanced photocatalytic hydrogen evolution, *ACS Catal.* 11 (2021) 6276–6289, <https://doi.org/10.1021/acscatal.0c05520>.

[38] Y. Li, S.W. Zuo, Q.H. Li, Hierarchical C-MoCS_x@MoS₂ nanoreactor as a chainmail catalyst for seawater splitting, *Appl. Catal. B-Environ.* 318 (2022), 121832, <https://doi.org/10.1016/j.apcatb.2022.121832>.

[39] Y.P. Zang, S.W. Niu, Y.S. Wu, Tuning orbital orientation endows molybdenum disulfide with exceptional alkaline hydrogen evolution capability, *Nat. Commun.* 10 (2019), 1217, <https://doi.org/10.1038/s41467-019-09210-0>.

[40] K.L. Zhou, Z.L. Wang, C.B. Han, Platinum single-atom catalyst coupled with transition metal/metal oxide heterostructure for accelerating alkaline hydrogen evolution reaction, *Nat. Commun.* 12 (2021), 3783, <https://doi.org/10.1038/s41467-021-24079-8>.

[41] W. Peng, Y. Wang, X.X. Yang, Co₉S₈ nanoparticles embedded in multiple doped and electrospun hollow carbon nanofibers as bifunctional oxygen electrocatalysts for rechargeable zinc-air battery, *Appl. Catal. B-Environ.* 268 (2020), 118437, <https://doi.org/10.1016/j.apcatb.2019.118437>.

[42] J.C. Li, W.Q. Li, H.W. Mi, Bifunctional oxygen electrocatalysis on ultra-thin Co₉S₈/MnS carbon nanosheets for all-solid-state zinc-air batteries, *J. Mater. Chem. A* 9 (2021) 22635–22642, <https://doi.org/10.1039/d1ta07019c>.

[43] X.J. Hu, T. Huang, Y.W. Tang, Three-dimensional graphene-supported Ni₃Fe/Co₉S₈ composites: Rational design and active for oxygen reversible electrocatalysis, *ACS Appl. Mater. Inter.* 11 (2019) 4028–4036, <https://doi.org/10.1021/acsmami.8b19971>.

[44] Y.Y. She, J. Liu, H.K. Wang, Bubble-like Fe-encapsulated N,S-codoped carbon nanofibers as efficient bifunctional oxygen electrocatalysts for robust Zn-air batteries, *Nano Res* 13 (2020) 2175–2182, <https://doi.org/10.1007/s12274-020-2828-3>.

[45] K. Du, L.F. Zhang, J.Q. Shan, Interface engineering breaks both stability and activity limits of RuO₂ for sustainable water oxidation, *Nat. Commun.* 13 (2022), 5448, <https://doi.org/10.1038/s41467-022-33150-x>.

[46] W. Liu, H. Liu, L.N. Dang, Amorphous cobalt-iron hydroxide nanosheet electrocatalyst for efficient electrochemical and photo-electrochemical oxygen evolution, *Adv. Funct. Mater.* 27 (2017) 1603904, <https://doi.org/10.1002/adfm.201603904>.

[47] N.K. Oh, J. Seo, S. Lee, Highly efficient and robust noble-metal free bifunctional water electrolysis catalyst achieved via complementary charge transfer, *Nat. Commun.* 12 (2021), 4606, <https://doi.org/10.1038/s41467-021-24829-8>.

[48] S.H. Liu, S.Z. Geng, L. Li, A top-down strategy for amorphization of hydroxyl compounds for electrocatalytic oxygen evolution, *Nat. Commun.* 13 (2022), 1187, <https://doi.org/10.1038/s41467-022-28888-3>.

[49] A.T. Swesi, J. Masud, M. Nath, Nickel selenide as a high-efficiency catalyst for oxygen evolution reaction, *Energy Environ. Sci.* 9 (2016) 1771–1782, <https://doi.org/10.1039/c5ee02463c>.

[50] L.C. Bai, S. Lee, X.L. Hu, Spectroscopic and electrokinetic evidence for a bifunctional mechanism of the oxygen evolution reaction, *Angew. Chem. Int. Ed.* 60 (2021) 3095–3103, <https://doi.org/10.1002/anie.202011388>.

[51] F. Dionigi, Z.H. Zeng, L. Sinev, In-situ structure and catalytic mechanism of NiFe and CoFe layered double hydroxides during oxygen evolution, *Nat. Commun.* 11 (2020), 2522, <https://doi.org/10.1038/s41467-020-16237-1>.

[52] C. Wei, Z.X. Feng, G.G. Scherer, Cations in octahedral sites: a descriptor for oxygen electrocatalysis on transition-metal spinels, *Adv. Mater.* 29 (2017), 1606800, <https://doi.org/10.1002/adma.201606800>.

[53] M. Retuerto, L. Pascual, F. Calle-Vallejo, Na-doped ruthenium perovskite electrocatalysts with improved oxygen evolution activity and durability in acidic media, *Nat. Commun.* 10 (2019), 2041, <https://doi.org/10.1038/s41467-019-09791-w>.